Sensorless Synchronous Reluctance Motor Drives: A Full-Speed Scheme using Finite-Control-Set MPC in a Projection Vector Framework

Anantaram Varatharajan
Department of Energy
Politecnico di Torino
Turin, Italy
anantaram.varatharajan@polito.it

Paolo Pescetto
Department of Energy
Politecnico di Torino
Turin, Italy
paolo.pescetto@polito.it

Gianmario Pellegrino
Department of Energy
Politecnico di Torino
Turin, Italy
gianmario.pellegrino@polito.it

***Abstract*—The paper presents a general framework valid for high frequency excitation based position observer for low speed sensorless control of synchronous reluctance machines. A finite control set model predictive control technique is proposed accordingly, exploiting the switching current ripple for position estimation. Position error due to cross-saturation is inherently accounted for. The proposed scheme is integrated with Adaptive Projection vector for Position error estimation (APP) for high speeds region through a simple fusion structure for smooth transition. Performance of proposed technique is validated on a 1.1 kW synchronous reluctance motor test bench.**

***Index Terms*—Sensorless control, model predictive control, synchronous reluctance machine**

I. Introduction

Thanks to the saliency of synchronous reluctance (SyR) machine, the position and speed estimation without an encoder or resolver becomes realizable. The fundamental wave excitation approaches based on back-emf are robust at medium and high speeds regions, but falter at low speeds and are unobservable at standstill. To circumvent this, the fundamental excitation scheme is usually supplemented with high frequency excitation schemes for sustained operation in zero to low speeds region.

The high frequency excitation schemes can be broadly classified into two categories: continuous and discontinuous excitation. The continuous excitation pertains to the periodic high frequency injection in the form of rotating or pulsating signals in stationary or synchronous reference frames for low speeds position estimation. A pulsating voltage injection along d-axis in synchronous reference frame is reported in [1]–[3] while rotating voltage injection in stationary reference frame is reported in [4], [5]. Compensation of position error owing to cross-saturation is addressed in [6]–[8]. To simplify the demodulation stage and bandwidth constraints, square wave voltage injection at close to switching frequency is explored in [9]–[11]; however, their feasibility is challenged in high inductance machines as the amplitude of injected voltage is a limited resource.

Multiple works on discontinuous excitation schemes sans periodic injection have been studied: [12], [13] proposes a modified PWM patterns and over-sampling for INFORM method, while [14] phase shifts PWM carrier waves to generate a rotating voltage at switching frequency. Intermittent test voltage vector injection is proposed in [15], [16]. Alternatively, finite control set model predictive control (FCS-MPC) assists current derivatives/ripples based approach as the full dc-link voltage appears across the motor terminals in a control period due to absence of modulators. The authors of [17] use model predictive current control and calculate the position error signal from the back-emf component, which is inadequate for low speeds operation. An optimization solver is used in [18] for MPC based position estimation which has a demerit of high steady-state error ($> 10^\circ$) under load, due to neglected effects of saturation; the results obtained do not justify the computational effort. Predictive torque control is used in [19] where the position error signal is computed in stationary reference frame; additional angle compensation curve is used to compensate for cross-saturation effects. The position error is observed to be quite large in the bounds of $\pm 20^\circ$. Position estimation in stationary reference frame with MPC is proposed in [20] which, besides being computationally elaborate, overlooks the impact of saturation and cross-saturation. Work [21] reports a comprehensive review of high frequency injection techniques.

Dealing with the medium to high speed range, numerous sensorless schemes based on fundamental excitation have been reported in literature [22]–[24]. Active flux based sensorless

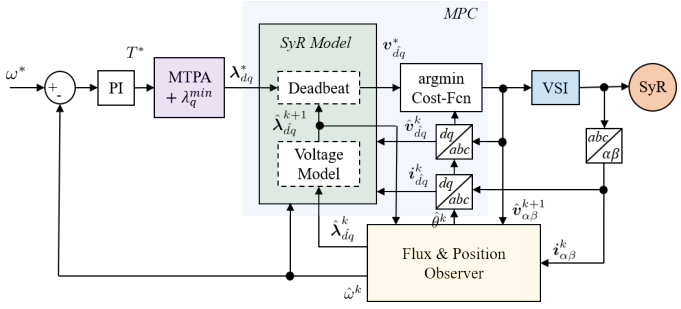

Fig. 1. Block diagram of the sensorless model predictive control scheme with flux and position observer.

control is widely studied in [5], [8], [25]; however, it suffers from instabilities at braking and very high speeds operation as expounded in [26], [27]. An Adaptive Projection vector for Position error estimation (APP) is proposed in [27] to ensure stability in all operating points. Fusion methods for smooth transitioning between the low and high speed models are reported in [5] [8].

The previous conference work [28] proposed a deadbeat FCS-MPC based sensorless control estimating position error from the discrepancy in incremental flux estimation between voltage and current models, for zero to low speeds region. In this work, such FCS-MPC algorithm is reformulated within the generalized context of projection vector framework, for the first time for position error construction in the low speed region, upon its introduction for fundamental excitation schemes [27]. Within such framework, the high frequency excitation position observer is integrated with a fundamental excitation scheme based on APP for high speeds region. The APP scheme stand valid at very high speeds for flux weakening and maximum torque per volt (MTPV) operations; however, they are deemed out of scope for this paper.

The section II introduces the machine model, control system notation and the model predictive control scheme with flux observer. Section III and IV presents the main contributions of the paper, summarized as follows:

- A general projection vector framework is developed for zero to low speeds region position estimation based on high frequency excitation. Its applicability to various signal injection schemes, including FCS-MPC is shown in section III.
- Accordingly, an injection-less scheme based on FCS-MPC is developed which inherently accounts for saturation and cross-saturation effects.
- In section IV, the proposed scheme is integrated with APP for high speeds region with a speed-dependent fusion coefficient for smooth transition.
- Parameter tuning guidelines are addressed for compatibility with plug & play and self-commissioning systems.

The section V presents the experimental validation of the proposed injection-less scheme and the dynamic performance on a 1.1 kW SyR motor test bench.

II. Sensorless Control System

The electrical rotor position is θ and the electrical angular speed is $\omega = s\,\theta$ where s is the differential operator $\mathrm{d}/\mathrm{d}t$. Estimated vectors are represented by the superscript $\hat{}$. The orthogonal rotational matrix is $\mathbf{J} = \left[\begin{smallmatrix} 0 & -1 \\ 1 & 0 \end{smallmatrix}\right]$ and $\mathbf{I}$ is the identity matrix.

The machine model is expressed in coordinates of *estimated rotor reference frame*, denoted by subscript $\hat{d}\hat{q}$, whose d-axis is at $\hat{\theta} = \theta - \tilde{\theta}$, where $\tilde{\theta}$ is the position error. Real space vectors will be used; for example, the stator current in estimated rotor reference frame is $\boldsymbol{i}_{\hat{d}\hat{q}} = [i_{\hat{d}}, i_{\hat{q}}]^{\mathrm{T}}$. Space vectors in stationary reference frame are denoted by subscript $\alpha\beta$. The block diagram illustrating an overview of motor control scheme is shown in the Fig. 1.

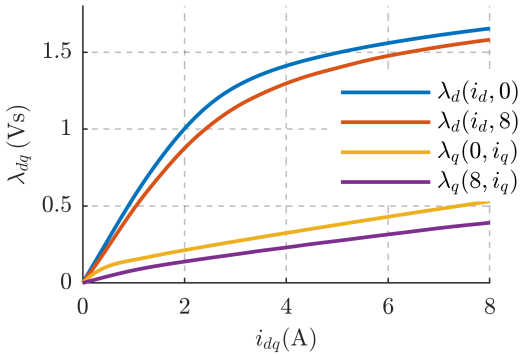

Fig. 2. Experimentally obtained flux maps lookup table, $\boldsymbol{\Lambda}$, of the SyR motor under test: $\boldsymbol{\lambda}_{dq} = \boldsymbol{\Lambda}(\boldsymbol{i}_{dq}) = \boldsymbol{L}^i \cdot \boldsymbol{i}_{dq}$

A. Mathematical Model of SyR Machine

The voltage equation of a SyR machine is expressed as

$$s\,\boldsymbol{\lambda}_{\hat{d}\hat{q}} = \boldsymbol{v}_{\hat{d}\hat{q}} - R_s \boldsymbol{i}_{\hat{d}\hat{q}} - \hat{\omega}\,\mathbf{J}\,\boldsymbol{\lambda}_{\hat{d}\hat{q}} \tag{1}$$

where R_s is the stator resistance and $\boldsymbol{\lambda}_{\hat{d}\hat{q}}$ is the stator flux linkage. The stator flux linkage and its time-derivative in terms of the incremental inductance $\boldsymbol{l}$ and apparent inductance $\boldsymbol{L}$ matrices in estimated reference frame are expressed as

$$\boldsymbol{\lambda}_{\hat{d}\hat{q}} = \mathrm{e}^{\mathbf{J}\tilde{\theta}}\,\boldsymbol{L}\,\mathrm{e}^{-\mathbf{J}\tilde{\theta}}\,\boldsymbol{i}_{\hat{d}\hat{q}} \tag{2a}$$

$$s\,\boldsymbol{\lambda}_{\hat{d}\hat{q}} = s\left(\mathrm{e}^{\mathbf{J}\tilde{\theta}}\,\boldsymbol{\lambda}_{dq}\right) = s\,\tilde{\theta}\cdot\mathbf{J}\,\boldsymbol{\lambda}_{\hat{d}\hat{q}} + \mathrm{e}^{\mathbf{J}\tilde{\theta}}\,\boldsymbol{l}\,s\left(\mathrm{e}^{-\mathbf{J}\tilde{\theta}}\,\boldsymbol{i}_{\hat{d}\hat{q}}\right) \tag{2b}$$

The components of inductance matrices are

$$\boldsymbol{l}(\boldsymbol{i}_{dq}) = \begin{bmatrix} l_d & l_{dq} \\ l_{dq} & l_q \end{bmatrix} \qquad \boldsymbol{L}(\boldsymbol{i}_{dq}) = \begin{bmatrix} L_d & 0 \\ 0 & L_q \end{bmatrix} \tag{3}$$

where l_d, l_q represents the incremental inductance along direct d and quadrature q-axis respectively while l_{dq} is the cross-saturation term. Apparent inductance are defined likewise. All quantities are a function of $\boldsymbol{i}_{dq}$. The electromagnetic torque is given by

$$T = \frac{3p}{2}\,\boldsymbol{i}_{\hat{d}\hat{q}}^{\mathrm{T}}\,\mathbf{J}\,\boldsymbol{\lambda}_{\hat{d}\hat{q}} \tag{4}$$

where p is the number of pole pairs.

B. Hybrid Flux Observer

The flux observer is implemented in stator reference frame, depicted in Fig. 4 and defined as

$$s\hat{\boldsymbol{\lambda}}_{\alpha\beta} = \boldsymbol{v}_{\alpha\beta} - R_s\boldsymbol{i}_{\alpha\beta} + \boldsymbol{G}_{\alpha\beta}\left(\mathrm{e}^{\mathbf{J}\hat{\theta}}\boldsymbol{L}^i\,\mathrm{e}^{-\mathbf{J}\hat{\theta}}\boldsymbol{i}_{\alpha\beta} - \hat{\boldsymbol{\lambda}}_{\alpha\beta}\right) \tag{5}$$

where $\boldsymbol{G}_{\alpha\beta}$ is a 2×2 gain matrix and $\boldsymbol{L}^i$ is the flux map lookup tables (LUTs) based current model apparent inductance in estimated rotor reference frame. State equation of flux observer in the estimated rotor reference frame is given by

$$s\,\hat{\boldsymbol{\lambda}}_{\hat{d}\hat{q}} = \boldsymbol{v}_{\hat{d}\hat{q}} - R_s\boldsymbol{i}_{\hat{d}\hat{q}} - \hat{\omega}\mathbf{J}\,\hat{\boldsymbol{\lambda}}_{\hat{d}\hat{q}} + \boldsymbol{G}\left(\boldsymbol{L}^i\,\boldsymbol{i}_{\hat{d}\hat{q}} - \hat{\boldsymbol{\lambda}}_{\hat{d}\hat{q}}\right) \tag{6}$$

where the gain matrix $\boldsymbol{G}$ is

$$\boldsymbol{G} = \mathrm{e}^{-\mathbf{J}\hat{\theta}}\,\boldsymbol{G}_{\alpha\beta}\,\mathrm{e}^{\mathbf{J}\hat{\theta}} \tag{7}$$

In this work, a diagonal gain matrix $\boldsymbol{G} = g\,\mathbf{I}$ is used; hence, the gain matrices are equivalent, $\boldsymbol{G} = \boldsymbol{G}_{\alpha\beta}$. The scalar value g determines the cross-over frequency from the predominance of current model - g rad/s or lower - to voltage model based observer - g rad/s or higher.

Let $\boldsymbol{\Lambda}$ denote the flux map LUTs of the machine under test $\boldsymbol{\lambda}_{dq} = \boldsymbol{\Lambda}(\boldsymbol{i}_{dq})$, shown in the Fig. 2. It is experimentally identified on a constant speed test-bench [29]. Accurate flux maps are assumed, i.e., $\hat{\boldsymbol{\Lambda}} = \boldsymbol{\Lambda}$. Nevertheless, as machine inductances vary with the operating point, and as $\boldsymbol{i}_{\hat{d}\hat{q}} \neq \boldsymbol{i}_{dq}$ under position error, the current model inductance $\boldsymbol{L}^i$ deviates from the real machine inductance $\boldsymbol{L}$. The current model apparent inductance is computed in real-time as

$$\boldsymbol{L}^i(\boldsymbol{i}_{\hat{d}\hat{q}}) \cdot \boldsymbol{i}_{\hat{d}\hat{q}} = \boldsymbol{\Lambda}(\boldsymbol{i}_{\hat{d}\hat{q}}) \tag{8}$$

Conversely, the real machine inductance $\boldsymbol{L}$ depends on the operating point $\boldsymbol{i}_{dq}$ as in (9).

$$\begin{aligned} \boldsymbol{L}(\boldsymbol{i}_{dq}) \cdot \boldsymbol{i}_{dq} &= \boldsymbol{\Lambda}(\boldsymbol{i}_{dq}) \\ \implies \boldsymbol{L}(\boldsymbol{i}_{dq}) \cdot \mathrm{e}^{-\mathbf{J}\tilde{\theta}}\, \boldsymbol{i}_{\hat{d}\hat{q}} &= \boldsymbol{\Lambda}(\mathrm{e}^{-\mathbf{J}\tilde{\theta}}\, \boldsymbol{i}_{\hat{d}\hat{q}}) \end{aligned} \tag{9}$$

Comparison of the former two expressions highlight phenomenon of position error induced inductance error. Linearizing (9) gives

$$\begin{aligned} \boldsymbol{L} \cdot (\boldsymbol{i}_{\hat{d}\hat{q}} - \tilde{\theta}\mathbf{J}\, \boldsymbol{i}_{\hat{d}\hat{q}}) &= \boldsymbol{\Lambda}(\boldsymbol{i}_{\hat{d}\hat{q}} - \tilde{\theta}\, \mathbf{J}\, \boldsymbol{i}_{\hat{d}\hat{q}}) \\ &\approx \boldsymbol{\Lambda}(\boldsymbol{i}_{\hat{d}\hat{q}}) - \tilde{\theta}\, \boldsymbol{l}\, \mathbf{J}\, \boldsymbol{i}_{\hat{d}\hat{q}} \end{aligned} \tag{10}$$

This is equivalent to the first-order Taylor series approximation [30]. On simplification using (8), the inductance model accounting parameter error (IMAP) is derived as

$$\boldsymbol{L} \approx \boldsymbol{L}^i + \tilde{\theta}\,(\boldsymbol{L}^i - \boldsymbol{l})\,\mathbf{J} \tag{11}$$

IMAP is introduced in [27] as improved inductance model. Note that the components of $\boldsymbol{L}^i$ are also denoted by the superscript i. Unlike apparent inductance, the incremental inductance is largely constant and invariant to small position error, i.e., $\boldsymbol{l}^i \approx \boldsymbol{l}$. The incremental inductance l_d is computed in real-time as

$$l_d(\boldsymbol{i}_{\hat{d}\hat{q}}) = \frac{\boldsymbol{\Lambda}(i_{\hat{d}} + \delta i_d, i_{\hat{q}}) - \boldsymbol{\Lambda}(i_{\hat{d}}, i_{\hat{q}})}{\delta i_d} \tag{12}$$

where δi_d is a small value (≈ 10 mA). The other incremental inductances are computed in a similar fashion.

C. Model Predictive Control Scheme

The key equations pertaining to a deadbeat type FCS-MPC in estimated synchronous rotor reference frame $\hat{d}\hat{q}$ are presented in (13)-(15). Controlled variables are the flux linkage components $\lambda_{\hat{d}}$ and $\lambda_{\hat{q}}$. The superscript k denotes the discrete k^{th} time instant.

To account for the unit digital delay, the observed state variable $\hat{\boldsymbol{\lambda}}^k_{\hat{d}\hat{q}}$ is estimated for the $k+1^{th}$ sampling instant as

$$\hat{\boldsymbol{\lambda}}^{k+1}_{\hat{d}\hat{q}} = \hat{\boldsymbol{\lambda}}^{k}_{\hat{d}\hat{q}} + T_s\Big(\boldsymbol{v}^k_{\hat{d}\hat{q}} - R_s \boldsymbol{i}^k_{\hat{d}\hat{q}} - \hat{\omega}\mathbf{J}\,\hat{\boldsymbol{\lambda}}^k_{\hat{d}\hat{q}}\Big) \tag{13}$$

where T_s is the sampling interval. This corresponds to the voltage model block in Fig. 1. The voltage $\boldsymbol{v}^k_{\hat{d}\hat{q}}$ in (13) is computed from the measured DC link voltage, incorporating dead-time compensation.

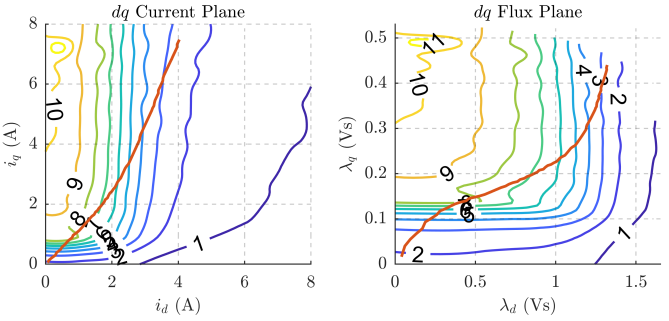

Fig. 3. Incremental saliency l_d/l_q of the 1.1 kW SyR machine under test: (a) in i_{dq} current plane; (b) in λ_{dq} flux plane. Red curve is the MTPA trajectory.

The deadbeat reference voltage $\boldsymbol{v}^*_{\hat{d}\hat{q}}$ that drives the error to zero at the next control cycle is given by

$$\boldsymbol{v}^*_{\hat{d}\hat{q}} = R_s\, \boldsymbol{i}^k_{\hat{d}\hat{q}} + \frac{\boldsymbol{\lambda}^*_{\hat{d}\hat{q}} - \hat{\boldsymbol{\lambda}}^{k+1}_{\hat{d}\hat{q}}}{T_s} + \hat{\omega}\,\mathbf{J}\,\hat{\boldsymbol{\lambda}}^{k+1}_{\hat{d}\hat{q}} \tag{14}$$

where $\boldsymbol{\lambda}^*_{dq}$ is the reference flux that corresponds to the commanded reference torque T^* from the speed control loop. The $T^* \rightarrow \boldsymbol{\lambda}^*_{dq}$ relationship is obtained by superimposing a minimum λ_q over the MTPA trajectory; the need for a minimum λ_q is to aid the sensorless control as discussed in the succeeding section. The resistive term in (14) is relatively insignificant and hence, the current quantities are not estimated for $k+1$ in the interest of computational efficiency.

The cost function to determine the voltage vector that is at the shortest Euclidean distance from the reference voltage (14) is given by

$$f(\boldsymbol{v}^{k+1}_{\hat{d}\hat{q},j}) = |\boldsymbol{v}^*_{\hat{d}\hat{q}} - \boldsymbol{v}^{k+1}_{\hat{d}\hat{q},j}| \tag{15a}$$

$$\boldsymbol{v}^{k+1}_{\hat{d}\hat{q}} = \underset{j=0,1..7}{\operatorname{argmin}}\, f(\boldsymbol{v}^{k+1}_{\hat{d}\hat{q},j}) \tag{15b}$$

where the notation $\boldsymbol{v}_{\hat{d}\hat{q},j}$ represents the six active vectors ($j = 1\ldots6$) and two zero vectors ($j = 0, 7$) of a two-level voltage source inverter in estimated rotor reference frame.

D. Saliency Analysis

Incremental saliency is defined as the ratio of incremental inductances l_d/l_q. All high frequency based sensorless techniques rely on incremental saliency for position estimation at zero to low speeds region.

Fig. 3 shows the incremental saliency of the machine under test in both dq current and dq flux planes. At no load, around the origin, saliency disappears due to the unsaturated ribs in the q-axis. This is circumvented by imposing a minimum flux in q-axis for a reliable presence of incremental saliency. Moreover, at very high loads, the saturation of d-axis reduces the saliency on MTPA trajectory as illustrated in Fig. 3. Hence, low speed sensorless drives should be wary of poor saliency regions for stable operation.

III. Low Speed Position Error Estimation

A. General Framework Development

The generalized high frequency based position error signal ϵ_h is defined as the projection of difference in voltage and current model high frequency flux estimates on a projection vector $\boldsymbol{\phi}_h$, expressed as

$$\epsilon_h = \boldsymbol{\phi}_h^{\mathrm{T}} \left(s\,\boldsymbol{\lambda}_{\hat{dq}} - \boldsymbol{l} \cdot s\,\boldsymbol{i}_{\hat{dq}} \right) \tag{16}$$

where derivatives represents the high frequency terms. The projection vector $\boldsymbol{\phi}_h$ has the dimension of V^{-1}.

At high frequencies, the approximation of observed high frequency flux to the real (voltage model) high frequency flux holds, $s\,\hat{\boldsymbol{\lambda}}_{\hat{dq}} \approx s\,\boldsymbol{\lambda}_{\hat{dq}}$. The term $s\,\boldsymbol{\lambda}_{\hat{dq}}$ in (16) is computed directly from (1) while the current model flux estimate $\boldsymbol{l} \cdot s\,\boldsymbol{i}_{\hat{dq}}$ is obtained from flux map LUTs.

To establish the relation of position error signal ϵ_h in (16) to position error $\tilde{\theta}$, the term $s\,\boldsymbol{i}_{\hat{dq}}$ is examined as

$$s\,\boldsymbol{i}_{\hat{dq}} = s\left(\mathrm{e}^{\mathbf{J}\tilde{\theta}}\boldsymbol{i}_{dq}\right) = s\,\tilde{\theta}\cdot\mathbf{J}\,\mathrm{e}^{\mathbf{J}\tilde{\theta}}\,\boldsymbol{i}_{dq} + \mathrm{e}^{\mathbf{J}\tilde{\theta}}\cdot s\,\boldsymbol{i}_{dq} \tag{17}$$

$$= \mathrm{e}^{\mathbf{J}\tilde{\theta}}\,\boldsymbol{l}^{-1}\,\mathrm{e}^{-\mathbf{J}\tilde{\theta}}\cdot s\,\boldsymbol{\lambda}_{\hat{dq}} + s\,\tilde{\theta}\cdot\mathrm{e}^{\mathbf{J}\tilde{\theta}}\left(\mathbf{J}\,\boldsymbol{L}^{-1} - \boldsymbol{l}^{-1}\mathbf{J}\right)\mathrm{e}^{-\mathbf{J}\tilde{\theta}}\,\boldsymbol{\lambda}_{\hat{dq}}$$

Derivative of position error is neglected, i.e., $s\,\tilde{\theta} = 0$. Linearizing (17) for small values of $\tilde{\theta}$ gives

$$s\,\boldsymbol{i}_{\hat{dq}} \approx \boldsymbol{l}^{-1}\cdot s\,\boldsymbol{\lambda}_{\hat{dq}} + \tilde{\theta}\left(\mathbf{J}\,\boldsymbol{l}^{-1} - \boldsymbol{l}^{-1}\mathbf{J}\right)\cdot s\,\boldsymbol{\lambda}_{\hat{dq}} \tag{18}$$

Substituting (18) in (16), the high frequency position error signal simplifies to

$$\epsilon_h = \boldsymbol{\phi}_h^{\mathrm{T}}\cdot\tilde{\theta}\left(\mathbf{J} - \boldsymbol{l}\,\mathbf{J}\,\boldsymbol{l}^{-1}\right)\cdot s\,\boldsymbol{\lambda}_{\hat{dq}} \tag{19a}$$

$$\mathbf{J} - \boldsymbol{l}\,\mathbf{J}\,\boldsymbol{l}^{-1} = \frac{1}{l_d\,l_q - l_{dq}^2}\begin{bmatrix} -l_{dq}(l_d + l_q) & l_d^2 - l_d\,l_q + 2\,l_{dq}^2 \\ -(l_q^2 - l_d\,l_q + 2\,l_{dq}^2) & l_{dq}(l_d + l_q) \end{bmatrix} \tag{19b}$$

It can be inferred from (19) that the error signal ϵ_h is always a function of the position error $\tilde{\theta}$, irrespective of the projection vector $\boldsymbol{\phi}_h$.

B. Applicability to Signal Injection Schemes

The general framework is applicable for sinusoidal and square-wave high frequency voltage injection schemes. The components of high frequency injected signal in estimated rotor reference frame are denoted by subscript $\hat{dq}h$.

For a pulsating voltage injection of magnitude v_h and frequency ω_h along $\hat{d}$ axis, the high frequency flux is given by

$$\boldsymbol{v}_{\hat{dq}h} = v_h\begin{bmatrix}\cos(\omega_h \mathrm{t})\\ 0\end{bmatrix} \implies \boldsymbol{\lambda}_{\hat{dq}h} = \frac{v_h}{\omega_h}\begin{bmatrix}\sin(\omega_h \mathrm{t})\\ 0\end{bmatrix} \tag{20}$$

As the derivative is an algebraic operator in high frequency domain, it is convenient to use the integral of (16) as

$$\epsilon_h = \boldsymbol{\phi}_h^{\mathrm{T}}\left(\frac{v_h}{\omega_h}\begin{bmatrix}\sin(\omega_h \mathrm{t})\\ 0\end{bmatrix} - \boldsymbol{l}\cdot\boldsymbol{i}_{\hat{dq}h}\right) \tag{21}$$

Consequently, the projection vector $\boldsymbol{\phi}_h$ takes the dimension of $(\mathrm{Vs})^{-1}$. Using (19) and (20), the error function (21) is equivalent to

$$\epsilon_h = \boldsymbol{\phi}_h^{\mathrm{T}}\cdot\tilde{\theta}\begin{bmatrix} -l_{dq}(l_d + l_q) \\ -(l_q^2 - l_d\,l_q + 2\,l_{dq}^2)\end{bmatrix}\frac{v_h\,\sin(\omega_h \mathrm{t})}{\omega_h(l_d l_q - l_{dq}^2)} \tag{22}$$

The d-axis signal in (22), being proportional to the cross-saturation term l_{dq}, is diminished in magnitude and unobservable at $i_d = 0$. Hence, the q-axis signal is preferred for reliability whose the corresponding projection vector is given by

$$\boldsymbol{\phi}_h = \begin{bmatrix}0 & \phi_{qh}\end{bmatrix}^{\mathrm{T}} \tag{23a}$$

$$\phi_{qh}^{-1} = -\frac{v_h\,(l_q^2 - l_d\,l_q + 2\,l_{dq}^2)}{\omega_h(l_d l_q - l_{dq}^2)} \tag{23b}$$

Ideally, the demodulation of error signal is equivalent to the position error as

$$\tilde{\theta} = \mathrm{LPF}\left(\epsilon_h \cdot 2\,\sin(\omega_h \mathrm{t})\right) \tag{24}$$

This approach is adopted in [8] [31]. The low pass filter in the demodulation stage (24) hinders the maximum achievable bandwidth of the position observer. Typically, the closed-loop bandwidth of position tracking loop is set to three times lower than the cutoff frequency of the low pass filter [7]. Moreover, additional low pass filters to retrieve fundamental current component unfavorably affects the current controller in vector control scheme. To alleviate these concerns, injection at near switching frequency has been extensively studied [9]–[11].

C. Proposed Sensorless Technique with MPC

Let the discrete time derivative function be represented the operator Δ as

$$\Delta x^k = \frac{1}{T_s}(x^k - x^{k-1}) \tag{25}$$

Owing to the nature of finite control set MPC, discrete voltage vectors are applied. The proposed scheme is based on the instantaneous machine response upon excitation with an active voltage vector.

The position error function (16) is reformulated in the context of MPC as the difference in voltage and current model flux ripple from the last switching actuation as

$$\epsilon_h^k = \boldsymbol{\phi}_h^{\mathrm{T}\,k}\left(\Delta\boldsymbol{\lambda}_{\hat{dq}}^k - \boldsymbol{l}\cdot\Delta\boldsymbol{i}_{\hat{dq}}^k\right) \tag{26}$$

The term $\Delta\boldsymbol{\lambda}_{\hat{dq}}^k$ is computed from the HFO while $\Delta\boldsymbol{i}_{\hat{dq}}^k$ is determined from measurements. The susceptibility of error function (26) to measurement noise should be addressed. Owing to the smaller inductance in q-axis, the current ripple Δi_q is generally higher than Δi_d and consequently, less gullible to measurement noise and current sensor resolution. Furthermore, the noise is amplified in $l_d\,\Delta i_d$ more than $l_q\,\Delta i_q$

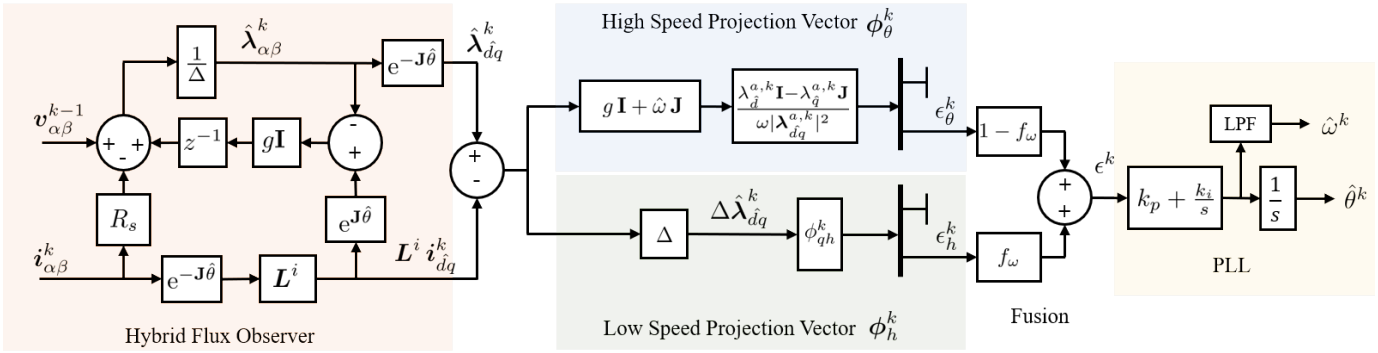

Fig. 4. Block diagram of the proposed sensorless technique highlighting the hybrid flux observer with low and high speed projection vectors relying on high frequency and fundamental excitation respectively, fusion mechanism and PLL.

since $l_d > l_q$. Hence, a projection vector along q-axis is preferred as

$$\boldsymbol{\phi}_h^k = \begin{bmatrix} 0 & \phi_{qh}^k \end{bmatrix}^{\mathrm{T}} \tag{27}$$

The gain ϕ_{qh}^k should be chosen such that $\epsilon_h = \tilde{\theta}$. To this end, in the context of MPC, the error function in (19) transforms to

$$\epsilon_h^k = \left(\boldsymbol{\phi}_h{}^k\right)^{\mathrm{T}} \cdot \tilde{\theta} \left(\mathbf{J} - \boldsymbol{l}\,\mathbf{J}\,\boldsymbol{l}^{-1}\right) \cdot \Delta\boldsymbol{\lambda}_{\hat{dq}}^k \tag{28}$$

From (27) and (28), it follows that ϕ_{qh} has a dimension of V^{-1} and takes the form

$$\phi_{qh}^k{}^{-1} = \frac{l_{dq}(l_d + l_q)}{l_d\, l_q - l_{dq}^2}\, \Delta\lambda_{\hat{q}}^k - \frac{l_q^2 - l_d\, l_q + 2\, l_{dq}^2}{l_d\, l_q - l_{dq}^2}\, \Delta\lambda_{\hat{d}}^k \tag{29}$$

At low speeds, the magnitude of active voltage vector is much greater than resistance and back-emf terms. Hence, for computational simplicity, $\Delta\boldsymbol{\lambda}_{\hat{dq}}^k \approx \boldsymbol{v}_{\hat{dq}}^{k-1}$ is adopted. Note that the term ϕ_{qh}^k is effectively a gain; therefore, the approximation will only marginally shift the bandwidth of observer but does not translate to steady-state error. Finally, the expression of term ϕ_{qh}^k in (29) is simplifies to

$$\phi_{qh}^k{}^{-1} \approx \frac{l_{dq}(l_d + l_q)}{l_d\, l_q - l_{dq}^2}\, v_{\hat{q}}^{k-1} - \frac{l_q^2 - l_d\, l_q + 2\, l_{dq}^2}{l_d\, l_q - l_{dq}^2}\, v_{\hat{d}}^{k-1} \tag{30}$$

D. Implementation Constraints

At low speeds, the control tends to impose a string of zero vectors in steady-state. This impedes the sensorless performance as the machine remains unexcited for a short span of time. Moreover, the quantity $\phi_{qh}{}^{-1}$ in (29) represents the strength of position error signal and must be large enough for a reliable position estimation.

To meet these requirements, two thresholds are defined:

- ϕ_{min}^{-1} is the minimum value of $|\phi_{qh}^k{}^{-1}|$ to be deemed reliable.
- N_{max} is the maximum permissible number of consecutive voltage vectors to have failed the threshold ϕ_{min}^{-1}.

The cost function is modified such that a hard constraint C is enabled once the threshold N_{max} is reached as

$$f(\boldsymbol{v}_{\hat{dq},j}^{k+1}) = |\boldsymbol{v}_{\hat{dq}}^* - \boldsymbol{v}_{\hat{dq},j}^{k+1}| + \left(n > N_{max}\right) C_j \tag{31}$$

where n is the count of consecutive instances of $|\phi_{qh}^k{}^{-1}| < \phi_{min}^{-1}$. When the limit N_{max} is exceeded, the hard constraint C_j functions to ensure that only those active voltage vectors $\boldsymbol{v}_{\hat{dq},j}^{k+1}$ that satisfy ϕ_{min}^{-1} are eligible for the next sampling instant. This is accomplished by computing the term $\phi_{qh,j}^{-1}$ for each of the six active vectors ($j = 1 \ldots 6$) and assigning a large penalty for the j^{th} vector if $|\phi_{qh,j}^{-1}| < \phi_{min}^{-1}$ as

$$C_j = \left(|\phi_{qh,j}^{-1}| \leq \phi_{min}^{-1}\right) \cdot \infty + \left(|\phi_{qh,j}^{-1}| > \phi_{min}^{-1}\right) \cdot 0 \tag{32}$$

For the applied voltage vectors having $|\phi_{qh}^k{}^{-1}| < \phi_{min}^{-1}$, the evaluation of error function is suspended with $\epsilon_h^k = 0$.

IV. Full-Speed Position Observer

The proposed full-speed flux and position observer scheme is described in Fig. 4. This includes the Hybrid Flux Observer and the position error evaluation through the low speed projections vector. In parallel, a high speed projection vector block evaluates the position error from fundamental model for high speeds region. The fusion and phase locked loop blocks complete the sensorless scheme, as described in the following.

A. High Speed Position Error Estimation

The Adaptive Projection vector for Position error estimation (APP) approach introduced in [27] is used for position observation at medium to high speed. Using the projection vector approach also for the fundamental excitation model of the machine, the generalized position error signal ϵ_θ is defined as the projection of difference in observed and current model flux estimates on the vector $\boldsymbol{\phi}_\theta$ as

$$\epsilon_\theta = \boldsymbol{\phi}_\theta^{\mathrm{T}} \left(\hat{\boldsymbol{\lambda}}_{\hat{dq}} - \boldsymbol{L}^i\, \boldsymbol{i}_{\hat{dq}}\right) \tag{33}$$

Through linear error dynamics of the state observer (6), the transfer function K_θ from the position error signal to the position error $\epsilon_\theta \to \tilde{\theta}$ is derived in [27] as

$$K_\theta = \frac{\epsilon_\theta}{\tilde{\theta}} = \boldsymbol{\phi}_\theta^{\mathrm{T}} \left(s\,\mathbf{I} + \boldsymbol{G} + \omega\mathbf{J}\right)^{-1} \left(s\,\mathbf{I} + \omega\mathbf{J}\right) \boldsymbol{\lambda}_{\hat{dq}}^a \tag{34}$$

where $\boldsymbol{\lambda}_{\hat{dq}}^a$ is the auxiliary flux vector. Using IMAP, the auxiliary flux vector is computed to [27]

$$\boldsymbol{\lambda}_{\hat{dq}}^a = \left(\mathbf{J}\,\boldsymbol{L}^i - \boldsymbol{l}\,\mathbf{J}\right) \boldsymbol{i}_{\hat{dq}} = \begin{bmatrix} (l_d - L_q^i)\, i_{\hat{q}} - l_{dq}\, i_{\hat{d}} \\ (L_d^i - l_q)\, i_{\hat{d}} + l_{dq}\, i_{\hat{q}} \end{bmatrix} \tag{35}$$

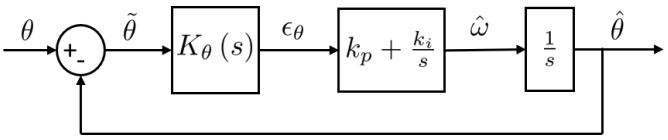

Fig. 5. Analysis of high speed closed loop transfer function of position observer

Thus, it follows from (34) that the projection vector to obtain $K_\theta = 1$ is given by

$$\boldsymbol{\phi}_\theta^{\mathrm{T}} = \frac{-1}{\omega\,|\boldsymbol{\lambda}^a_{\hat{dq}}|^2}\;\boldsymbol{\lambda}^{a^{\mathrm{T}}}_{\hat{dq}}\,\mathbf{J}\left(s\,\mathbf{I} + \boldsymbol{G} + \omega\,\mathbf{J}\right) \tag{36}$$

The derivative term in (36) does not have a major impact on the closed loop position observer as demonstrated in the next section. Hence, the projection vector is simplified to

$$\boldsymbol{\phi}_\theta^{\mathrm{T}} = \frac{-1}{\omega\,|\boldsymbol{\lambda}^a_{\hat{dq}}|^2}\;\boldsymbol{\lambda}^{a^{\mathrm{T}}}_{\hat{dq}}\,\mathbf{J}\left(\boldsymbol{G} + \omega\,\mathbf{J}\right) \tag{37}$$

The projection vector in (37) is referred to as APP. For a constant gain g flux observer, the APP technique is shown to have better stability than the active-flux based position estimation in [27]. Furthermore, the APP is immune to stator resistance variations and non-ideal inverter compensation as demonstrated in [32].

Since the high speed error estimation relies on fundamental quantities, the switching constraint (32) is obsolete and the cost function reverts back to (15).

B. Fusion Structure

The position observer is designed to transition from low to high speed model at the cross-over frequency g, akin to the flux observer. To refrain from sharp discontinuous transition and chattering, the two position estimation models are fused together with a linear speed dependent fusion coefficient f_ω, expressed as

$$\epsilon^k = f_\omega \cdot \epsilon^k_h + \left(1 - f_\omega\right) \cdot \epsilon^k_\theta \tag{38a}$$

$$f_\omega = \begin{cases} 1, & \text{if } |\hat{\omega}^k| < g - \omega_g \\ 0, & \text{if } |\hat{\omega}^k| > g + \omega_g \\ \frac{g+\omega_g-|\hat{\omega}^k|}{2\omega_g}, & \text{otherwise} \end{cases} \tag{38b}$$

where the term ω_g signifies the span of transition on either sides of cross-over frequency g. The fusion coefficient f_ω is designed to ensure smooth transition over the span of speeds $g - \omega_g$ to $g + \omega_g$.

C. Phase Locked Loop

A conventional phased locked loop (PLL) with a proportional-integral (PI) controller is employed to drive the observer error signal ϵ^k to zero as

$$\hat{\omega} = k_p\,\epsilon + \int k_i\,\epsilon\,\mathrm{d}t \qquad \hat{\theta} = \int \hat{\omega}\,\mathrm{d}t \tag{39}$$

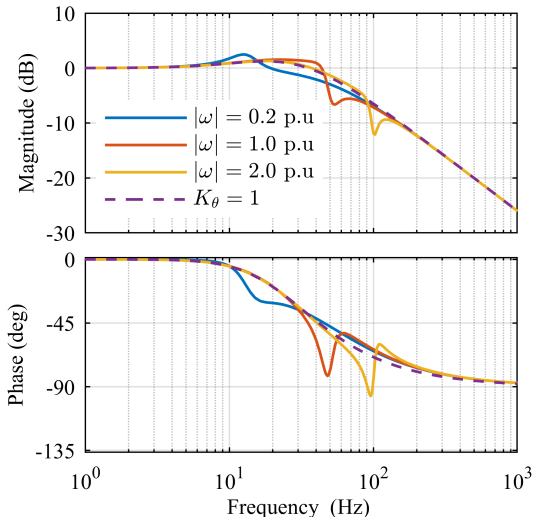

Fig. 6. Frequency response plot of closed loop position observer (41) for simplified projection vector (37) at three different operating speeds; dotted lines correspond to the ideal projection vector with derivative term (36). Parameters: $g = 2\pi \cdot 10$ rad/s, $\Omega_\omega = 2\pi \cdot 25$ rad/s.

where k_p and k_i are the respective gains. The gains of the PLL are tuned for a critically damped response considering $\epsilon = \tilde{\theta}$ by placing the two poles at $s = -\Omega_\omega$ as

$$k_p = 2\,\Omega_\omega \qquad k_i = \Omega_\omega^2 \tag{40}$$

It is of interest to analyze the dynamics of PLL, in particular, for high speed model. The block diagram of closed loop position observer is shown in Fig. 5 whose transfer function is given by

$$\frac{\hat{\theta}(s)}{\theta(s)} = \frac{(sk_p + k_i)\,K_\theta(s)}{s^2 + (sk_p + k_i)\,K_\theta(s)} \tag{41}$$

For $\boldsymbol{G} = g\,\mathbf{I}$ and using the projection vector (37), the transfer function K_θ in (34) reduces to

$$K_\theta = \frac{s^2 + g^2 + \omega^2 + s\,g}{(s+g)^2 + \omega^2} \tag{42}$$

Note that K_θ is a function of angular speed and is independent of operating point $\boldsymbol{i}_{dq}$. The frequency response plot of (41) at different operating speeds for simplified projection vector (37) is shown in the Fig. 6; also juxtaposed is the frequency response of ideal projection vector with the derivative term (36). Notice that the closed loop bandwidth is only marginally altered by the absence of derivative term, justifying the simplification.

D. Calibration of Gains

The flux observer gain is set to $g = 2\,\pi \cdot 10$ rad/s (300 rpm). For a precise position estimation at low speeds, it is desired that the error function is evaluated, at the least, once every mechanical degree. This results in $N_{max} = 5$ at the angular speed of g rad/s. Beyond g, the dominance of high speed model comes into effect. The threshold $\phi^{-1}_{min} = 60$ V

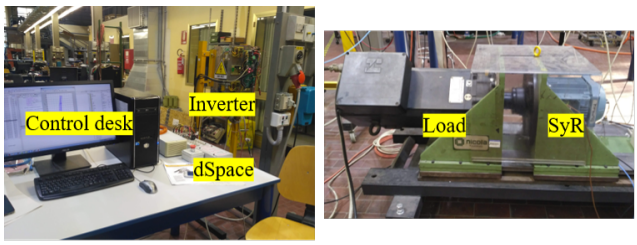

Fig. 7. Experimental Setup of 1.1 kW SyR motor under test on a dspace DS1103 control platform running at a sampling frequency of 10 kHz.

TABLE I
MOTOR PARAMETERS

Parameters	Symbol	Values	Units
Rated power	P_n	1.1	kW
Rated speed	ω_n	1500	rpm
Rated torque	T_n	7.1	Nm
Rated voltage	V_n	340	V
Rated current	I_n	2.3	A
Pole pairs	p	2	-
Stator resistance	R_s	4.5	Ω
Shaft inertia	J	0.04	kgm^2

is set to around 10% of DC link voltage. The transition span of the fusion model is set to $\omega_g = 2\,\pi \cdot 2$ rad/s.

The position observer poles are placed at $\Omega_\omega = 2\,\pi \cdot 25$ rad/s; the estimated speed is low-pass filtered at $2\,\pi \cdot 25$ rad/s. The poles of PI speed controller of SyR machine are placed for a critically damped response at $2\,\pi \cdot 1$ rad/s. A minimum flux $\lambda_q^{min} = 0.2$ Vs is imposed for saliency and fundamental excitation at no-load. Unless mentioned otherwise, the following results adhere to aforementioned parameters.

V. EXPERIMENTAL RESULTS

A. Test-bench Setup

The proposed sensorless scheme is validated experimentally on a 1.1 kW SyR motor on a dspace DS1103 control platform running at a sampling frequency of 10 kHz. A picture of the setup is shown in Fig. 7. The parameters of the SyR motor under test are tabulated in Table I. The SyR machine is sensorless speed controlled while the load torque is imposed by an auxiliary drive.

B. Test for Dynamic Stiffness

A challenging scenario for a low speed sensorless control is to sustain a rated torque step at standstill. In the Fig. 8(a), a heavy transient of twice the rated torque is imposed at standstill condition. The position error is stable with an error less than $\approx 5^\circ$ at steady-state. The small error at standstill is likely due to secondary saliences as the flux map LUTs is an average model computed from constant speed test [29]. The high speed model is subjected to similar test in Fig. 8(b) at 750 rpm (0.5 p.u); negligible position error is observed. Besides, the two tests show similar sag in angular speed during transients.

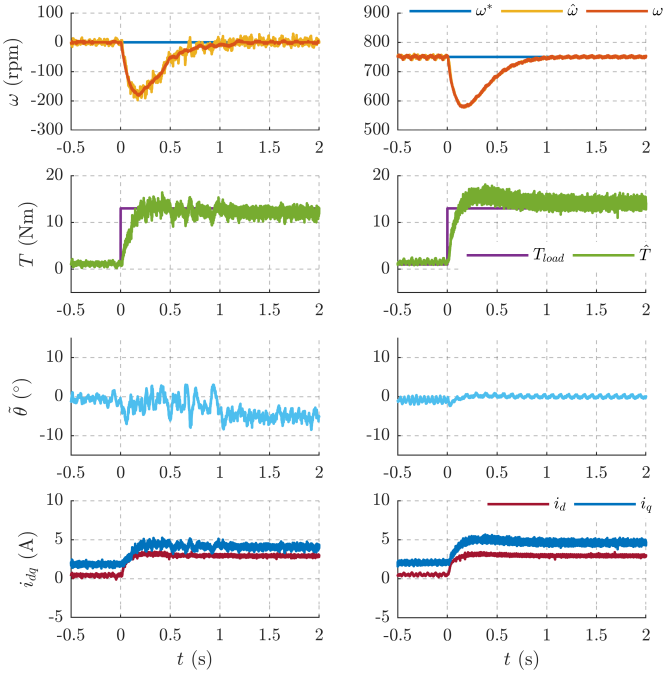

Fig. 8. Torque step of $0 \rightarrow 2$ p.u to test for dynamic stiffness with speed controller poles at $2\,\pi \cdot 1$ rad/s: (a) Low speed model at standstill condition $\omega^* = 0$; (b) High speed model at $\omega^* = 0.5$ p.u (750 rpm).

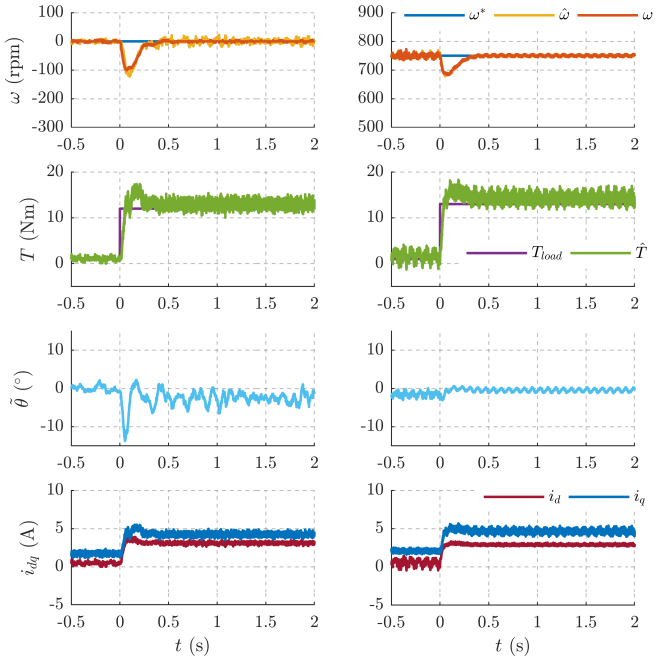

Fig. 9. Torque step of $0 \rightarrow 2$ p.u to test for dynamic stiffness with speed controller poles at $2\,\pi \cdot 2.5$ rad/s: (a) Low speed model at standstill condition $\omega^* = 0$; (b) High speed model at $\omega^* = 0.5$ p.u (750 rpm).

The tests in Fig. 8 are repeated for a higher bandwidth speed controller whose the poles are shifted from $2\,\pi \cdot 1$ rad/s to $2\,\pi \cdot 2.5$ rad/s, shown in the Fig. 9. To curtail the high frequency noise, the position observer poles are lowered from $2\,\pi \cdot 25$

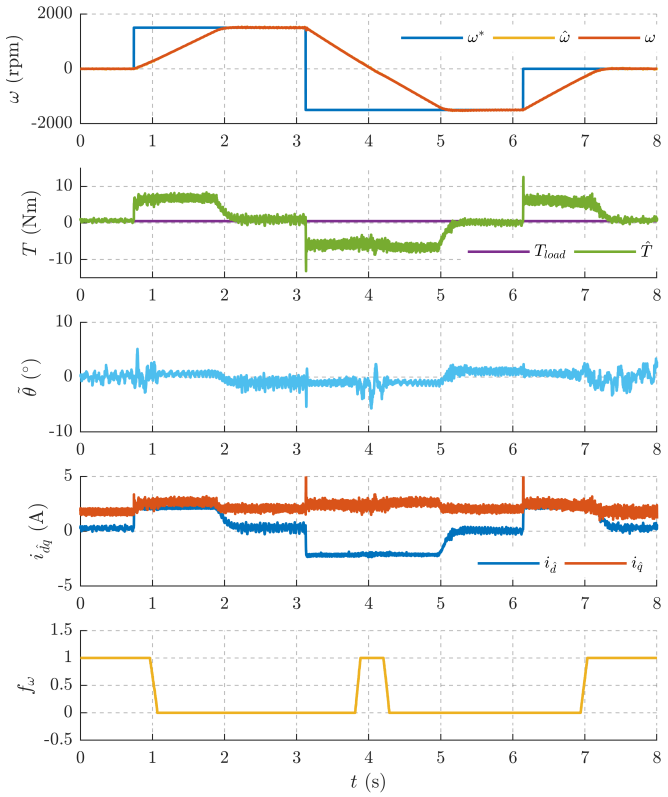

Fig. 10. Dynamic performance analysis: speed step 0 → 1 p.u and speed reversal 1 → -1 p.u at no load.

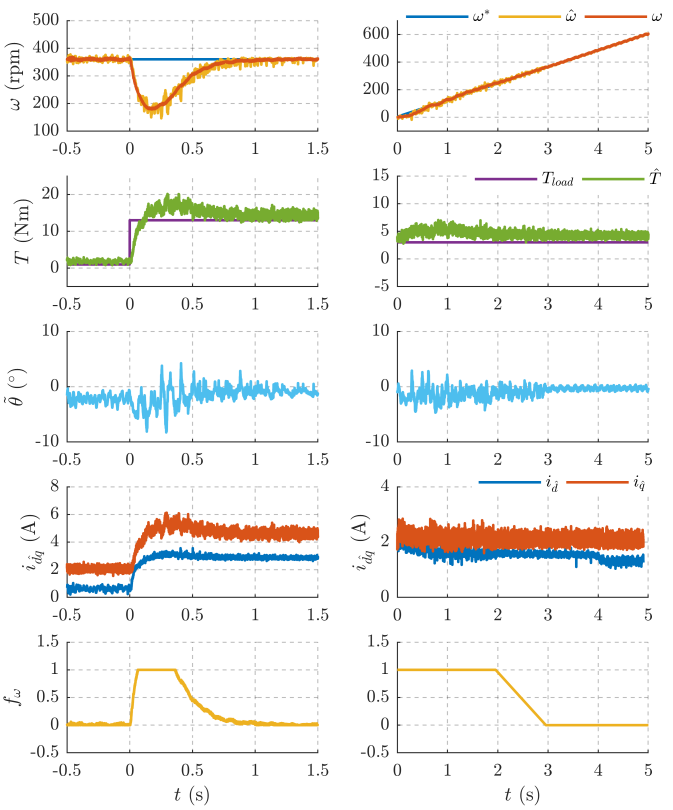

Fig. 11. Analysis of fusion: (a) Torque step at upper-bound speed of fusion window, $g + \omega_g$, to demonstrate transient performance; (b) Slow speed ramp to highlight the smoothness of transition.

rad/s to $2\pi \cdot 15$ rad/s which corresponds to a bandwidth of 37 Hz. Same scales are retained for ease of comparison. Peak transient position error is around 15°. The sag in speed is observed to decrease by a factor of 2 while the settling time is improved by a factor of 3.

C. Speed Transients

To demonstrate the dynamic performance, a step change in speed reference from 0 → 1500 rpm (1 p.u) and subsequently, speed reversal from 1500 →-1500 rpm are reported in Fig. 10. Negligible transient and steady-state position error is observed. The fusion coefficient f_ω signifies relative dominance of the two models.

D. Fusion

To illustrate the dynamic performance in the fusion region, a torque step in load of 1 p.u is applied in Fig. 11(a). The operating speed of machine is the upper-bound of fusion window, $g + \omega_g$. At $t = 0$s, the control abruptly transitions to the low speed model as pointed out by the fusion coefficient f_ω. Stability is retained.

A slow speed ramp is applied at a load torque of 0.5 p.u in Fig. 11(b) to illustrate the smooth transitioning between the models. The position error in Fig. 11(b) reflects transition where the high frequency noise is largely suppressed after $t = 3$s once fundamental excitation based estimation gains dominance.

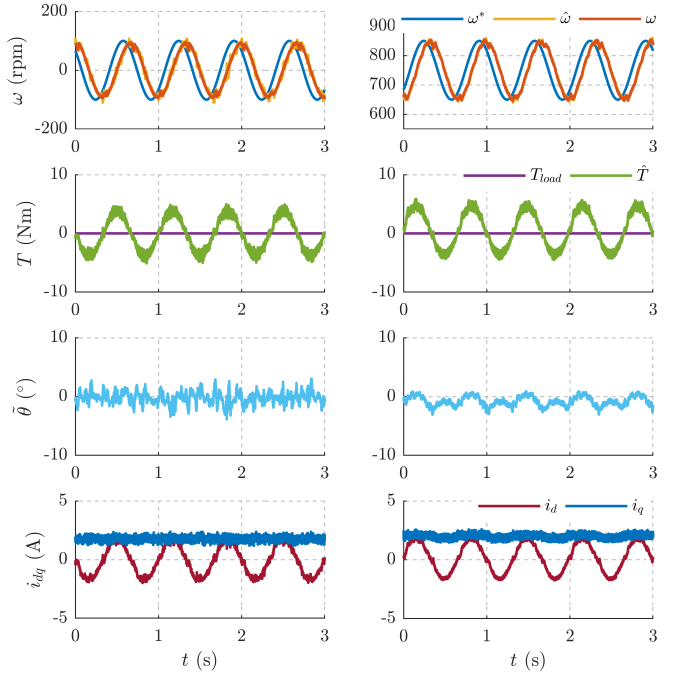

Fig. 12. Sinusoidal speed reference disturbances at 1.5 Hz: (a) Low speed model at standstill condition mean ω^* = 0; (b) High speed model at mean ω^* = 0.5 p.u (750 rpm).

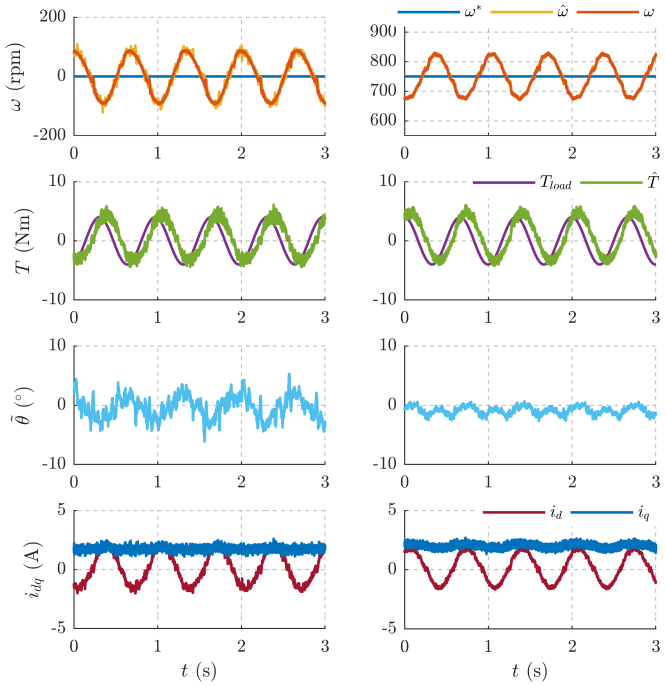

Fig. 13. Sinusoidal load torque disturbances at 1.5 Hz with speed controller poles at $2\pi \cdot 1$ rad/s: (a) Low speed model at standstill condition $\omega^* = 0$; (b) High speed model at $\omega^* = 0.5$ p.u (750 rpm).

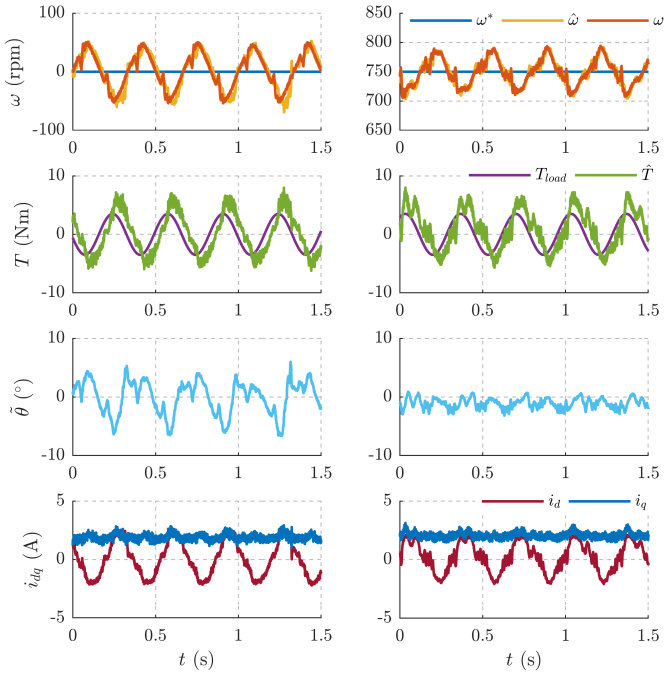

Fig. 14. Sinusoidal load torque disturbances at 3 Hz with speed controller poles at $2\pi \cdot 2.5$ rad/s: (a) Low speed model at standstill condition $\omega^* = 0$; (b) High speed model at $\omega^* = 0.5$ p.u (750 rpm).

E. Speed Control Bandwidth Analysis

To comment on the capability of proposed control to track disturbances, a sinusoidal speed reference is imposed at standstill to validate the low-speed sensorless model, as reported in Fig. 12(a). At a disturbance frequency of 1.5 Hz, the estimated speed is phase shifted by 45° from the reference speed. Similar behavior is observed at 750 rpm when the high speed model prevails, as shown in Fig. 12(b). In either case, the position error is negligible.

A second test regards sinusoidal disturbances in load torque injected at standstill conditions, reported in Fig. 13(a). At 1.5 Hz, the estimated torque lags the load torque by an angle of 45°. On Repeating the test at 750 rpm for high speed model in Fig. 13(b), identical behavior is discerned. The position error remains negligible.

These tests conclude that the control is capable of tracking disturbances either in load torque or in reference speed up to 1.5 Hz for the speed controller with poles at $2\pi \cdot 1$ rad/s. Shifting the poles to $2\pi \cdot 2.5$ rad/s increases the tracking frequency to 3 Hz as demonstrated in Fig. 14 where disturbances in load torque is injected at standstill and half-rated speed, analogous to the test in Fig. 13. Should higher bandwidth be desired, the gains of speed controller can be increased at the cost of increase in torque ripples due to discrete nature of FCS-MPC.

VI. Conclusion

Within the framework of projection vectors, this paper presents a sensorless technique for operation in all speeds without dedicated high frequency signal injection. Position estimate at low speeds is extracted from the switching actuation of FCS-MPC while the high speed model relies on flux observer error through APP scheme. A fusion coefficient is introduced for linear speed dependent transition between the two models.

The proposed technique is validated on a 1.1 kW SyR motor test bench; the position error is confined to $< 5°$ electrical during heavy load transients at standstill. Good dynamic performance is observed in speed step and speed reversal tests with seamless transition between the models. Furthermore, the control shows good resilience and tracks sinusoidal disturbances in load torque and speed reference commands.

References

[1] L. Harnefors and H. P. Nee, "A general algorithm for speed and position estimation of AC motors," *IEEE Transactions on Industrial Electronics*, vol. 47, no. 1, pp. 77–83, 2000.

[2] J.-H. Jang, J.-I. Ha, M. Ohto, K. Ide, and S. K. Sul, "Analysis of permanent-magnet machine for sensorless control based on high-frequency signal injection," *IEEE Transactions on Industry Applications*, vol. 40, no. 6, pp. 1595–1604, 2004.

[3] A. Piippo, M. Hinkkanen, and J. Luomi, "Analysis of an Adaptive Observer for Sensorless Control of Interior Permanent Magnet Synchronous Motors," *IEEE Transactions on Industrial Electronics*, vol. 55, no. 2, pp. 570–576, 2008.

[4] P. L. Jansen and R. D. Lorenz, "Transducerless position and velocity estimation in induction and salient AC machines," *IEEE Transactions on Industry Applications*, vol. 31, no. 2, pp. 240–247, 1995.

[5] S. C. Agarlita, I. Boldea, and F. Blaabjerg, "High-frequency-injection-assisted 'active-flux'-based sensorless vector control of reluctance synchronous motors, with experiments from zero speed," *IEEE Transactions on Industry Applications*, vol. 48, no. 6, pp. 1931–1939, 2012.

[6] J. I. Ha, K. Ide, T. Sawa, and S. K. Sul, "Sensorless rotor position estimation of an interior permanent-magnet motor from initial states," *IEEE Transactions on Industry Applications*, vol. 39, no. 3, pp. 761–767, 2003.

[7] T. Tuovinen and M. Hinkkanen, "Adaptive Full-Order Observer With High-Frequency Signal Injection for Synchronous Reluctance Motor Drives," *IEEE Journal of Emerging and Selected Topics in Power Electronics*, vol. 2, no. 2, pp. 181–189, 2014.

[8] A. Yousefi-Talouki, P. Pescetto, G. Pellegrino, and I. Boldea, "Combined Active Flux and High-Frequency Injection Methods for Sensorless Direct-Flux Vector Control of Synchronous Reluctance Machines," *IEEE Transactions on Power Electronics*, vol. 33, no. 3, pp. 2447–2457, 2018.

[9] Y. D. Yoon, S. K. Sul, S. Morimoto, and K. Ide, "High-bandwidth sensorless algorithm for AC machines based on square-wave-type voltage injection," *IEEE Transactions on Industry Applications*, vol. 47, no. 3, pp. 1361–1370, 2011.

[10] F. J. Barnard, W. T. Villet, and M. J. Kamper, "Hybrid Active-Flux and Arbitrary Injection Position Sensorless Control of Reluctance Synchronous Machines," *IEEE Transactions on Industry Applications*, vol. 51, no. 5, pp. 3899–3906, 2015.

[11] C. Hwang, Y. Lee, and S. K. Sul, "Analysis on Position Estimation Error in Position-Sensorless Operation of IPMSM Using Pulsating Square Wave Signal Injection," *IEEE Transactions on Industry Applications*, p. 1, 2018.

[12] E. Robeischl and M. Schroedl, "Optimized INFORM measurement sequence for sensorless PM synchronous motor drives with respect to minimum current distortion," *IEEE Transactions on Industry Applications*, vol. 40, no. 2, pp. 591–598, 2004.

[13] M. Hofer, M. Nikowitz, and M. Schroedl, "Sensorless control of a reluctance synchronous machine in the whole speed range without voltage pulse injections," in *2017 IEEE 3rd International Future Energy Electronics Conference and ECCE Asia (IFEEC 2017 - ECCE Asia)*, 2017, pp. 1194–1198.

[14] M. Mamo, K. Ide, M. Sawamura, and J. Oyama, "Novel rotor position extraction based on carrier frequency component method (CFCM) using two reference frames for IPM drives," *IEEE Transactions on Industrial Electronics*, vol. 52, no. 2, pp. 508–514, 2005.

[15] G. Xie, K. Lu, S. K. Dwivedi, J. R. Rosholm, and F. Blaabjerg, "Minimum-Voltage Vector Injection Method for Sensorless Control of PMSM for Low-Speed Operations," *IEEE Transactions on Power Electronics*, vol. 31, no. 2, pp. 1785–1794, 2016.

[16] R. Morales-Caporal and M. Pacas, "Suppression of saturation effects in a sensorless predictive controlled synchronous reluctance machine based on voltage space phasor injections," *IEEE Transactions on Industrial Electronics*, vol. 58, no. 7, pp. 2809–2817, jul 2011.

[17] M. Preindl and E. Schaltz, "Sensorless model predictive direct current control using novel second-order PLL observer for PMSM drive systems," *IEEE Transactions on Industrial Electronics*, vol. 58, no. 9, pp. 4087–4095, sep 2011.

[18] S. Nalakath, Y. Sun, M. Preindl, and A. Emadi, "Optimization-Based Position Sensorless Finite Control Set Model Predictive Control for IPMSMs," *IEEE Transactions on Power Electronics*, vol. 33, no. 10, pp. 8672–8682, 2018.

[19] P. Landsmann, D. Paulus, P. Stolze, and R. Kennel, "Saliency based encoderless Predictive Torque Control without signal injection for a reluctance synchronous machine," in *Proceedings of 14th International Power Electronics and Motion Control Conference EPE-PEMC 2010*, 2010, pp. S1–10–S1–17.

[20] L. Rovere, A. Formentini, A. Gaeta, P. Zanchetta, and M. Marchesoni, "Sensorless Finite-Control Set Model Predictive Control for IPMSM Drives," *IEEE Transactions on Industrial Electronics*, vol. 63, no. 9, pp. 5921–5931, 2016.

[21] F. Briz and M. W. Degner, "Rotor Position Estimation," *IEEE Industrial Electronics Magazine*, vol. 5, no. 2, pp. 24–36, 2011.

[22] R. D. Lorenz and K. W. Van, "High-Resolution Velocity Estimation for All-Digital, ac Servo Drives," *IEEE Transactions on Industry Applications*, vol. 27, no. 4, pp. 701–705, 1991.

[23] S. Morimoto, K. Kawamoto, M. Sanada, and Y. Takeda, "Sensorless control strategy for salient-pole PMSM based on extended EMF in rotating reference frame," *IEEE Transactions on Industry Applications*, vol. 38, no. 4, pp. 1054–1061, 2002.

[24] Y. Lee and S. K. Sul, "Model-Based Sensorless Control of an IPMSM With Enhanced Robustness Against Load Disturbances Based on Position and Speed Estimator Using a Speed Error," *IEEE Transactions on Industry Applications*, vol. 54, no. 2, pp. 1448–1459, 2018.

[25] I. Boldea, M. C. Paicu, G. Andreescu, and F. Blaabjerg, ""Active Flux" DTFC-SVM Sensorless Control of IPMSM," *IEEE Transactions on Energy Conversion*, vol. 24, no. 2, pp. 314–322, 2009.

[26] M. Hinkkanen, S. E. Saarakkala, H. A. A. Awan, E. Mölsä, and T. Tuovinen, "Observers for Sensorless Synchronous Motor Drives: Framework for Design and Analysis," *IEEE Transactions on Industry Applications*, vol. 54, no. 6, pp. 6090–6100, 2018.

[27] A. Varatharajan and G. Pellegrino, "Sensorless Synchronous Reluctance Motor Drives: A General Adaptive Projection Vector Approach for Position Estimation," *IEEE Transactions on Industry Applications*, pp. 1–10, 2019.

[28] A. Varatharajan, P. Pescetto, and G. Pellegrino, "Injectionless Sensorless Control of Synchronous Reluctance Machine for Zero to Low Speeds Region," in *2018 IEEE 9th International Symposium on Sensorless Control for Electrical Drives (SLED)*, 2018, pp. 72–77.

[29] E. Armando, R. I. Bojoi, P. Guglielmi, G. Pellegrino, and M. Pastorelli, "Experimental identification of the magnetic model of synchronous machines," *IEEE Transactions on Industry Applications*, vol. 49, no. 5, pp. 2116–2125, 2013.

[30] M. Morandin, D. Da Ru, S. Bolognani, and N. Bianchi, "An Integrated Starter-Alternator Based on a Sensorless Synchronous Reluctance Machine Drive," in *2015 IEEE Vehicle Power and Propulsion Conference, VPPC 2015 - Proceedings*, 2015, pp. 1–6.

[31] A. Yousefi-Talouki, P. Pescetto, and G. Pellegrino, "Sensorless Direct Flux Vector Control of Synchronous Reluctance Motors Including Standstill, MTPA, and Flux Weakening," *IEEE Transactions on Industry Applications*, vol. 53, no. 4, pp. 3598–3608, 2017.

[32] A. Varatharajan and G. Pellegrino, "Sensorless Synchronous Reluctance Motor Drives: A Sensitivity Analysis Framework and Design to Achieve Stator Resistance Immunity," in *2019 IEEE 10th International Symposium on Sensorless Control for Electrical Drives (SLED)*, 2019, pp. 1–6.